CERN-PPE/90-133
20 September 1990

DIFFRACTION DISSOCIATION OF NUCLEI IN 450 GeV/c PROTON–NUCLEUS COLLISIONS

The HELIOS Collaboration

T. Åkesson[3], S. Almehed[6], A.L.S. Angelis[20], H. Atherton[3], P. Aubry[8], H.W. Bartels[4], G. Beaudoin[8], J.M. Beaulieu[8], H. Beker[3], O. Benary[18], D. Bettoni[3,a], V. Bisi[19], I. Blevis[21], H. Bøggild[3,b], W. Cleland[12], M. Clemen[12], B. Collick[12], F. Corriveau[7], S. Dagan[18], K. Dederichs[3,c], S. Dell'Uomo[13], P. Depommier[8], R.C.E. Devenish[3,d], N. DiGiacomo[5], S. DiLiberto[13], J.R. Dodd[20], B. Dolgoshein[10], A. Drees[4], H. En'yo[3], B. Erlandsson[17], M.J. Esten[20], C.W. Fabjan[3], M.A. Faessler[3,c], P. Fischer[4], Z. Fraenkel[21], A. Gaidot[15], F. Gibrat-Debu[15], P. Giubellino[19], P. Glässel[4], U. Goerlach[3], R. Haglund[6], L.A. Hamel[7], H. van Hecke[5], V. Hedberg[3], R. Heifetz[18], A. Holscher[4], B. Jacak[5], G. Jarlskog[6], S. Johansson[6], H. Kraner[2], V. Kroh[4], F. Lamarche[7], C. Leroy[7], D. Lissauer[12,18], G. London[15], B. Lorstad[6], A. Lounis[8], F. Martelli [19,h] A. Marzari-Chiesa[19], M. Masera[19], M.A. Mazzoni[3], E. Mazzucato[7], N.A. McCubbin[14], P. McGaughey[5], F. Meddi[13], U. Mjornmark[6], M.T. Muciaccia[1], S. Muraviev[9], M. Murray[12], M. Neubert[4], S. Nilsson[17], L. Olsen[2], Y. Oren[18], J.P. Pansart[15], Y.M. Park[12], A. Pfeiffer[4], F. Piuz[3], V. Polychronakos[2], G. Poulard[3], M. Price[3], D. Rahm[2], L. Ramello[19], L. Riccati[19], G. Romano[16], G. Rosa[13], L. Sandor[3], J. Schukraft[3], M. Sekimoto[3,e], M. Seman[3,f], A. Shmeleva[9], V. Sidorov[11], S. Simone[1], Y. Sirois[7], H. Sletten[3], S. Smirnov[10], W. Sondheim[5], H.J. Specht[4], I. Stumer[2], J.W. Sunier[5], V. Tcherniatin[10], H.H. Thodberg[3], J. Thompson[12], V. Tikhomirov[9], I. Tserruya[21], G. Vasseur[15], R. Veenhof[3,g], R. Wigmans[3], W.J. Willis[3] and P. Yepes[7]

Abstract

Diffractive dissociation of nuclei (Be, Al, W) in collisions with 450 GeV/c protons, pA $\rightarrow$ pX, has been measured with the HELIOS spectrometer at the CERN Super Proton Synchrotron. The dependence of the single-diffraction cross-section σ_{SD} on the nuclear mass A can be parametrized as $\sigma_{SD} = (3.8 \pm 0.3)\,\mathrm{mb} \times A^{0.35\pm0.02}$, showing the peripheral nature of the process. The differential cross-section $d\sigma_{SD}/dt$ is exponential with the slope parameter, increasing from 6.2 ± 0.4 $(\mathrm{GeV}/c)^{-2}$ for beryllium to 7.9 ± 0.5 $(\mathrm{GeV}/c)^{-2}$ for tungsten. The slope parameter also increases with increasing mass M_X of the diffractively produced state. The rapidity, multiplicity, and transverse-momentum distributions of the particles of the diffractively produced state X show a longitudinal phase-space population and are remarkably insensitive to the nuclear mass. This, together with the $A^{1/3}$ dependence of σ_{SD}, suggests that the dominant process of nuclear diffractive excitation is the dissociation of single nucleons.

(Submitted to Zeitschrift für Physik C)

[1]) University of Bari and INFN, I-70100 Bari, Italy.
[2]) Brookhaven National Laboratory, Upton, NY 11973, USA.
[3]) CERN, CH-1211 Geneva 23, Switzerland.
[4]) University of Heidelberg, D-6900 Heidelberg, Fed. Rep. Germany.
[5]) Los Alamos National Laboratory, Los Alamos, NM 87 544, USA.
[6]) University of Lund, S-223 62 Lund, Sweden.
[7]) McGill University, Montreal H3A 2T8, Quebec, Canada.
[8]) University of Montreal, Montreal HC3 3J7, Quebec, Canada.
[9]) Lebedev Institute of Physics, SU-117924 Moscow, USSR.
[10]) Institute of Physics and Engineering, SU-115409 Moscow, USSR.
[11]) Institute of Nuclear Physics, SU-630 090 Novosibirsk, USSR.
[12]) University of Pittsburgh, Pittsburgh PA 15260, USA.
[13]) University of Rome 'La Sapienza' and INFN, I-00185 Rome, Italy.
[14]) Rutherford Appleton Laboratory, Didcot OX1 OQX, UK.
[15]) DPhPE, CEN–Saclay, F-91191 Gif-sur-Yvette, France.
[16]) University of Salerno and INFN, I-84100 Salerno Italy.
[17]) University of Stockholm, S-113 46 Stockholm, Sweden.
[18]) University of Tel Aviv, Ramat Aviv 9978, Israel.
[19]) University of Turin and INFN, I-10100 Turin, Italy.
[20]) University College London, London WC1E 6BT, UK.
[21]) Weizmann Institute, 76 100 Rehovot, Israel.
Visitor at CERN from:
[a]) University of Syracuse, Syracuse, NY 13244-1130, USA.;
[b]) Niels Bohr Institute, DK-2100 Copenhagen, Denmark.
[c]) Ludwig-Maximilians-Universität, D-8000 Munich 40, Fed. Rep. Germany.
[d]) Oxford University, Oxford OX1 3NP, UK.
[e]) Institute of Nuclear Study, Tokyo 188, Japan.
[f]) Slovak Academy of Sciences, CS-04353 Košice, Czechoslovakia.
[g]) NIKHEF-H, NL-1009 DB Amsterdam, The Netherlands.
[h]) 'Angelo Della Riccia' Fellow.

1 INTRODUCTION

Elastic scattering of hadrons at high energies reveals a pattern that is strikingly similar to the Fraunhofer diffraction of classical waves—in particular of light—on an opaque disk. The analogy is fully exploited in models called 'optical' or 's-channel', which provide a good description of elastic hadron diffraction.

Inelastic diffraction of hadrons, however, has no analogy in classical optics. In the process of single-diffraction dissociation in pp interactions, one of the incoming protons remains in its ground state, receiving only a small recoil momentum in the reference system in which it was at rest before the interaction. The second proton is excited to a higher mass and dissociates. This process has been extensively studied for pp interactions from Proton Synchrotron to ISR energies [1],[2] and for $p\bar{p}$ interactions at the CERN $p\bar{p}$ Collider. In the framework of optical models, it has been described in the following way. The wave function of one of the incoming protons is taken as a coherent superposition of various components (e.g. parton states with different parton numbers and configurations [3]). Because of the different absorption probabilities of the various components, the composition of the final-state wave function is altered in the interaction, leading to non-zero elements in the transition matrix to the individual components. Thus the components are 'filtered into existence' by their different absorption probabilities, and the total cross-section is determined by the dispersion of these probabilities. Optical models are capable of explaining the total diffraction cross-section and the momentum transfer (t-)dependence of elastic and inelastic diffraction. The latter is related to the profile of the average absorption dispersion as a function of the impact parameter.

The observed dependence of the pp invariant inelastic diffraction cross-section, $\mathrm{d}^2\sigma/\mathrm{d}M_X^2\mathrm{d}t$, on the mass M_X of the excited proton is simple for masses above the resonance region: it is proportional to M_X^{-2}, at fixed t. This dependence has not been explained within s-channel models but is predicted from the triple-Pomeron diagram [1] in the framework of the complementary Reggeon-exchange (or 't-channel') models.

Thus in the light of the two complementary approaches, inelastic pp diffraction is viewed as a process that is sensitive either to properties of the parton structure of the proton or to the properties of the inelastic Pomeron–proton vertex.

Suppose one of the incoming protons is replaced by a nucleus. Still limiting our discussion to single-diffraction dissociation, there are two distinct possibilities depending on whether the proton or the nucleus is excited. The first case, $pA \rightarrow XA$, is sensitive to the same physical parameters as those studied in pp diffraction: the parton structure of the proton or the inelastic Pomeron–proton vertex. The difference, however, is that the coherence condition is more restrictive. The maximum allowed momentum transfer in this case is given by the inverse nuclear (instead of proton) radius, as the whole nucleus

is required to recoil elastically. This process has been studied in some experiments in the hope of extracting information about the cross-sections of excited hadrons (p or π) in nuclear matter [4].

The other possible process—high-mass excitation of the nucleus, pA $\rightarrow$ pX—has not been studied in an experiment and, moreover, has not attracted a lot of theoretical interest so far [5]. In the light of our present understanding of pp diffraction, it is natural to wonder whether a study of this process can teach us more about the parton structure of nuclei or, alternatively, about the inelastic interaction of the Pomeron with nuclear matter.

These questions stimulated the carrying out of an experiment at the CERN Super Proton Synchrotron (SPS). It has been performed with the HELIOS detector using a proton beam of 450 GeV/c momentum. The primary interests of the HELIOS research programme are to study the production of lepton pairs in hadronic collisions (NA34/1) [6] and to search for new phenomena in nucleus–nucleus collisions (NA34/2) [7]. Although not designed for the experiment presented here, the apparatus could be used with only small modifications of the standard configuration.

This paper is organized as follows: the experimental set-up is described in Section 2, and the data-taking and analysis in Section 3. The experimental results are presented in Section 4, and these are discussed further in Section 5.

2 EXPERIMENTAL SET-UP

The components of the HELIOS spectrometer used for this measurement are shown in Fig. 1 and are described below.

2.1 Target region

The lepton part of the HELIOS programme requires an extremely small and very well collimated proton beam, referred to as the 'microbeam'. This beam was also used for the present data. It is collimated to about 50 μm base width and a divergence of 0.2 mrad at the target. Incident protons are defined by the coincidence of two scintillation counters (B1 and B2) located 25 cm upstream of the target. The targets used were 1 cm radius disks of aluminium, beryllium, and tungsten, of thickness 8%, 10%, and 10%, respectively, of an interaction length. The charged multiplicity in the region[1] $3.0 < \eta < 5.0$ was measured by the Silicon Pad Detector (SiPad in Fig. 1), which is an array of 400 silicon pad segments [8]. The scintillation counter B9, covering $0.2 \leq \eta \leq 2.2$, was added to

[1]In the following, all rapidities and pseudorapidities are given in the laboratory (target) rest system, unless otherwise stated.

the HELIOS set-up for this measurement in order to trigger on particles in the backward rapidity region.

2.2 Forward tracking

For $\eta > 3$, the momentum measurement and the vertex definition for charged secondaries are provided by a spectrometer consisting of a high-resolution drift chamber (DC1), followed by a dipole magnet (0.2 T·m), and by two further drift chambers (DC2 and DC3). Each chamber provides about 40 track points from wires with several azimuthal orientations to enable reconstruction of space points. The gas used is CO_2 (80%) + C_2H_6 (20%), which has low diffusion and is operated at low drift velocity (9.5 μm/ns) for optimum resolution. Under data-taking conditions, a spatial resolution of approx. 130 μm is achieved. Full details of the design and performance of the drift chambers are given in Ref. [9]. The momentum resolution of the spectrometer is $\sigma(p)/p^2 = 0.009\ (\mathrm{GeV}/c)^{-1}$ at $p \approx 10\,\mathrm{GeV}/c$, and the vertex resolution is 1.3 cm in the beam direction and 200 μm in the transverse coordinates.

The central regions of the drift chambers are insensitive, so through-going beam particles do not give signals. However, these regions are large enough to include also the diffractively scattered proton, which is of prime interest here. Accordingly, DC3 was displaced laterally by 1 cm so that the diffractively scattered proton passed through the active part of this chamber.

2.3 Calorimeter coverage

The HELIOS experiment has a set of calorimeters that give essentially 4π coverage in the centre-of-mass system. The calorimeters are described in detail in Refs. [10] and [11].

The region $-0.1 < \eta < 2.9$ is covered by a 'box' of calorimeter modules located about 120 cm from the target. The region $-0.1 < \eta < 2.3$ is covered by uranium/copper/scintillator modules with longitudinal readout after 6.4 radiation lengths and at the full depth of about 4 interaction lengths. The readout is divided into 574 towers of approx. 20 cm × 20 cm, matched to the transverse size of a hadronic shower. The electromagnetic resolution of these modules is approx. $25\%/\sqrt{E(\mathrm{GeV})}$, and the hadronic resolution is $45\%\text{–}60\%/\sqrt{E(\mathrm{GeV})}$. The region $2.3 < \eta < 2.9$ is covered by the iron/scintillator yoke of the dipole magnet used for forward tracking (subsection 2.2). The readout is divided into 24 azimuthal sectors of 15° each. The electromagnetic resolution is approx. $25\%/\sqrt{E(\mathrm{GeV})}$, and the hadronic resolution is around $70\%/\sqrt{E(\mathrm{GeV})}$.

The calorimeter coverage in the very forward region, $\eta > 3$, is provided by a uranium/liquid-argon calorimeter (ULAC) positioned downstream from the spectrometer used for forward tracking (subsection 2.2). The ULAC is described in detail in Ref. [12].

The electromagnetic section of 18 radiation lengths has 'pad' readout with a pad size of 2 cm × 2 cm. In the hadronic section of 4.0 absorption lengths, the readout is through 25 mm wide strips at different azimuthal orientations. The electromagnetic and hadronic resolutions of the ULAC are about $13\%/\sqrt{E(\mathrm{GeV})}$ and $50\%/\sqrt{E(\mathrm{GeV})}$, respectively.

Any shower leakage through the ULAC is absorbed in further uranium/copper/scintillator modules, of the same type as the one used in the 'box' region.

3 DATA-TAKING AND ANALYSIS

3.1 Event sample and trigger

Diffractive interactions studied in this experiment have the following topology: the incident proton is scattered, losing only a small fraction of its momentum in the collision with a target nucleus, whilst the latter is diffractively excited to high mass and subsequently undergoes hadronic fragmentation. The experiment runs at the highest proton momentum available from the SPS, 450 GeV/c, in order to cover an excitation mass range that is as wide as possible. Three different nuclear targets (Be, Al, W) have been chosen so as to assess the target mass dependence of this particular diffractive channel. Their thickness (about 10% of an interaction length) is a compromise in order to achieve as high an interaction rate as possible while keeping re-interactions in the target at a low level. With a beam rate of 5×10^4 s, about 10^4 interactions occur during the spill time of 2.4 s, of which about 100 are selected and recorded by the trigger and data-acquisition system.

Triggers on diffractive interactions make use of their distinctive kinematic properties: owing to the small four-momentum transfer, the scattered proton is found in the very forward direction close to beam rapidity; accordingly, the particles emitted from the dissociating nucleus have limited longitudinal momenta and are located at backward rapidity. One finds a region which is kinematically excluded ('rapidity gap').

Trigger information comes from three detector components. A minimum-bias interaction (INT) requires a valid beam (VB), which is the coincidence of the two beam counters B1 and B2 (VB = B1·B2), and at least one charged particle in the backward rapidity range covered by the scintillation counter B9 (B9: $N_{\mathrm{ch}} \geq 1$ in $\eta < 2.2$; INT = VB·B9). The multiplicity in the rapidity gap region is measured by the Silicon Pad Detector, and events with more than two charged particles registered are rejected (SP2: $N_{\mathrm{ch}} \leq 2$ in $3.0 \leq \eta \leq 5.0$). In order to enhance high-mass diffraction events, the transverse-energy deposit in the uranium calorimeters—Box, Wall, and MagCal—is measured and compared with two threshold values, ET1 and ET2 (ET1: $E_\perp > 3.5$ GeV in $\eta \leq 2.9$; ET2: $E_\perp > 6.0$ GeV in $\eta \leq 2.9$).

Three types of diffraction triggers are formed from these inputs. A minimum-bias diffraction trigger (DFX) is given by the coincidence INT·SP2; two high-mass diffrac-

tion triggers require, in addition, transverse energies above the cited thresholds (DF1= DFX·ET1; DF2=DFX·ET2). For normalization purposes, events are also recorded with a pure VB trigger as well as with INT triggers. Calibration of the various detectors further requires 'empty' events taken with a random trigger outside the spill time (MT).

The data-taking was performed during a 24-hour period in September 1987, recording in total about 3.0×10^5 events with the different types of diffraction triggers.

3.2 Event reconstruction

The HELIOS set-up allows complete reconstruction of diffractive events, i.e. to measure the scattered forward proton and to detect single particles produced in the backward fragmentation region simultaneously.

The data are processed using the standard HELIOS analysis software, including the track reconstruction in the drift chambers and the evaluation of the energy deposits in the calorimeters. In the backward pseudorapidity range, $-0.1 \leq \eta \leq 2.9$, a clustering algorithm then determines the position and the energy of neutral as well as charged particles from the individual energy depositions in the 574 hadronic and 492 electromagnetic calorimeter towers. For particles with $E_{\mathrm{kin}} \geq 200$ MeV, the average reconstruction efficiency is 85%. In the range $\eta > 2.7$, the drift chambers achieve a tracking efficiency of 90%. Neutral particles in this area deposit their energy in the ULAC behind the DCs.

Rapidity and pseudorapidity distributions of the particles of the diffractively produced system can be obtained by combining the single-particle detection in calorimeters and drift chambers.

The trajectory of the leading proton is determined in DC3, whilst its momentum p is measured in the forward calorimeters with a resolution of 3% (15 GeV/c). The combined information yields the transverse momentum $p_\perp$ and the four-momentum transfer squared t:

$$p_\perp = p \tan\vartheta \simeq p\vartheta\,, \qquad -t = p_0\, p\, \vartheta^2\,,$$

where p_0 is the incident momentum of 450 GeV/c and ϑ is the deflection angle in the interaction. Since the incoming 'microbeam' is well collimated, ϑ can be determined with an accuracy of $\sigma_\vartheta = 0.22$ mrad, a convolution of the angular resolution of DC3 (0.08 mrad for a known vertex position), and the beam divergence. This is then also the limiting factor for the t-resolution, $\sigma(t) = 0.2$ GeV/$c \times \sqrt{t}$, with t measured in (GeV/c)^2.

The most accurate way to obtain the momentum loss $\Delta p_\parallel$ of the diffractively scattered proton is to calculate the sum of longitudinal momenta of the backward particles:

$$\Delta p_\parallel = C(\Delta p_\parallel) \sum_{n_i} p_{\parallel i}\,.$$

The correction coefficients $C(\Delta p_\parallel)$ can be accurately determined on a statistical basis by correlating $\Delta p_\parallel$ with the momentum of the leading proton as measured in the forward calorimeters. The values of these coefficients are found to be close to one. The resolution is $\sigma(\Delta p_\parallel)/\Delta p_\parallel \simeq 0.25 x_F^3$ for $\Delta p_\parallel > 8$ GeV/c. The Feynman x_F (in the proton–nucleon c.m.s.-frame) is obtained directly:

$$(1 - x_F) = \left(\frac{\Delta p_\parallel}{p_0}\right)_{\rm cms} \simeq \frac{\Delta p_\parallel}{p_0} .$$

The mass M_X of the diffractively produced system can be calculated as:

$$M_X^2 \simeq m_p^2 + s(1 - x_F) ,$$

where $\sqrt{s}$ is the centre-of-mass energy of the proton–nucleon collision. An alternative, but less accurate, method is to calculate the invariant mass of all detected particles except the forward proton.

3.3 Selection of diffractive interactions

The diffraction trigger (DFX) suppresses the non-diffractive background by about a factor of 5. A further filtering of all the data is achieved by applying four sets of cuts:

1. *General cuts*: Events with data-decoding errors or missing information are rejected. Pile-up rejection is achieved by requiring that the energy deposition in the beam counters (B1 and B2) be less than three times the most probable $\mathrm{d}E/\mathrm{d}x$, and by requiring that the total energy registered in all calorimeters be between 375 GeV and 500 GeV. Events are identified as off-target interactions if any track reconstructed in DC1 or DC2 points more than 5 cm upstream or more than 10 cm downstream from the target. If a track vertex is reconstructed, it has to be within a fiducial cylinder of 1 cm radius and 4 cm length around the target.

2. *Leading proton identification*: The trajectory is required to be reconstructed in DC3. The longitudinal momentum loss $\Delta p_\parallel$ is required to be less than 35 GeV/c, corresponding to $x_F \geq 0.925$. A lower limit of the transverse momentum, $p_\perp > 0.1$ GeV/c, is imposed to suppress quasi-elastic[2] and elastic background, which show a steeper t-distribution [2] ($p_\perp^2 \simeq x_F t$). An upper cut-off, $p_\perp < 0.6$ GeV/c, is applied in order to reduce background from inelastic reactions with high-energy leading particles [13].

3. *Backward system*: At least two clusters with a minimum energy of 0.5 GeV are required to be reconstructed in the backward calorimeters ($\eta < 2.9$).

[2]Quasi-elastic scattering in nuclear collisions means elastic scattering on the nucleon level with subsequent break-up of the nucleus.

4. *Rapidity gap*: A rapidity gap is imposed at the trigger level (subsection 3.1), and is strengthened off-line by rejecting events with tracks in either DC1 or DC2 at angles smaller than 17.5 mrad ($\eta = 4.75$). The minimum angle at which a track can be seen in DC1 or DC2 is about 5 mrad ($\eta = 6.0$), so events are required to have no charged particles in $4.75 < \eta < 6.0$. (Note that the leading proton is not detected in DC1 or DC2.) Events with neutral particles in this region are suppressed by imposing an upper limit of 30 GeV on the electromagnetic energy in the ULAC.

After these selection criteria, which result in a further data reduction by a factor of 20, the sample of diffractive events (N_{DFX}) is 2605 events for Be, 464 for Al, and 1425 for W.

3.4 Normalization and background estimation

Events satisfying the VB trigger condition were recorded during the data-taking, and passed through the 'general cuts' described in subsection 3.3; the number of events thus selected gives directly the total beam flux on the target. From this and from details of target, the observed rate for any process can be converted into a cross-section. Hence:

$$\frac{\mathrm{d}^2\sigma_n(x_{\mathrm{F}},t)}{\mathrm{d}x_{\mathrm{F}}\mathrm{d}t} = \frac{\mathrm{d}^2N_{\mathrm{DFX}}}{\mathrm{d}x_{\mathrm{F}}\mathrm{d}t}\,\frac{1}{N_{\mathrm{VB}}}\,\frac{\xi_{\mathrm{DFX}}}{\xi_{\mathrm{VB}}}\,\frac{A}{N_{\mathrm{A}}\,\rho\,l}\,,$$

where N_{A}, l, ρ, and A denote Avogadro's constant, the length of the target, its density, and its atomic number, respectively. The values N_{DFX} and N_{VB} are the numbers of events recorded under the DFX and VB trigger conditions and surviving off-line cuts, and ξ_i are the 'downscale factors' applied directly at the trigger level. It should be noted that inefficiencies of the trigger and the data-acquisition system cancel out in the above expression.

In order to deduce the single-diffraction cross-section $\mathrm{d}^2\sigma_{\mathrm{SD}}/\mathrm{d}x_{\mathrm{F}}\mathrm{d}t$, the non-diffractive background must be subtracted and the remaining cross-section corrected for the losses of diffractive events due to trigger and off-line cuts:

$$\frac{\mathrm{d}^2\sigma_{\mathrm{SD}}}{\mathrm{d}x_{\mathrm{F}}\mathrm{d}t} = \left(\frac{\mathrm{d}^2\sigma_n}{\mathrm{d}x_{\mathrm{F}}\mathrm{d}t} - \frac{\mathrm{d}^2\sigma_{\mathrm{background}}}{\mathrm{d}x_{\mathrm{F}}\mathrm{d}t}\right)\frac{1}{\varepsilon_{\mathrm{cut}}(x_{\mathrm{F}},t)}\,.$$

The evaluation of the acceptance correction coefficients $\varepsilon_{\mathrm{cut}}(x_{\mathrm{F}},t)$ will be discussed in subsection 3.5. The inelastic non-diffractive background in the data sample is estimated by using the IRIS Monte Carlo event generator [14], with its diffractive component [15] explicitly inhibited. After simulating the trigger conditions and the detector response, these Monte Carlo events are filtered by the same cuts as those for the diffraction data. The remaining background contribution, integrated over $(1 - x_{\mathrm{F}}) < 0.075$, and $0.01 < t < 0.36$ $(\mathrm{GeV}/c)^2$, before acceptance corrections, is 0.3 mb for Be, 0.5 mb for Al, and

1.4 mb for W. Although the systematic uncertainty in the Monte Carlo estimation is large, the impact on the final result is small since the background is less than 5% of the single-diffraction cross-section.

Diffractive events in which the beam particle is inelastically excited form another potential source of background, especially if target diffraction occurs as well (double diffraction). Both cases have been estimated with the 'two-step' Monte Carlo model, which is described in the next subsection. The result is that events with single diffraction of beam particles are rejected with an efficiency of more than 99% owing to the rapidity gap condition and the backward energy requirement; of the double-diffractive events, 2.5% pass the selection cuts. In pp collisions the cross-section for double diffraction has been measured to be 1.5 mb at $s = 900$ GeV^2 [1]. Assuming a target dependence of $A^{1/3}$, as found for single diffraction (see subsection 4.3), we estimate the background contribution from double diffraction to be 0.1 mb for Be and Al, and 0.2 mb for W.

Other potential sources of background are non-interacting or elastically scattered protons accompanied by unassociated background tracks. These events are subtracted on a statistical basis by making a comparison with a set of data taken without target. The background contribution from this source is 0.1 mb for Be, 0.2 mb for Al, and 1.0 mb for W.

3.5 Monte Carlo and efficiency corrections

In order to study the acceptance corrections $\varepsilon(x_F, t)$, diffractive events are generated by Monte Carlo simulation. To construct such an event, a leading proton is generated with a four-momentum transfer squared t and a Feynman x_F according to the distributions measured for pp diffraction [2]. These two variables determine the kinematics of the fragmentation system, such as mass M_X and average rapidity y_X, the only free choice being the fragmentation mode. Here, one can take advantage of the similarity to the fragmentation of inelastic reactions at $\sqrt{s} = M_X$ [16], [17] by using standard Monte Carlo programs to generate the final-state system of particles. We used IRIS [14], ISAJET [18], and a program that includes intranuclear cascading of secondary particles [19].

Alternatively, a phenomenological approach is followed, using the available information on fragmentation in diffractive interactions, i.e. the average charged-particle multiplicity has a standard KNO distribution [2]; the decay mode is $p_\perp$-limited [16] with an average $\langle p_\perp \rangle$ adjusted to 340 MeV/c according to our measurements. The charged particles are decomposed into protons and pions according to measurements of inelastic reactions at correspondingly low energies ($\sqrt{s} = M_X$) [20]. The number of neutral particles (photons and neutrons) is dominated by the π^0 multiplicity, which is taken to be half of the charged-pion multiplicity.

However, we observed that all generators, including the phenomenological model, give a lower multiplicity and a larger average rapidity than are observed in the data. A practical way to achieve the good agreement that is necessary in order to obtain reliable acceptance coefficients is to split a p–nucleus diffractive interaction of a given longitudinal momentum loss $\Delta p_{\parallel}$ into two consecutive p–nucleon diffractive interactions with momentum losses $\Delta p_{\parallel_1}$ and $\Delta p_{\parallel_2}$, so that $\Delta p_{\parallel} = \Delta p_{\parallel_1} + \Delta p_{\parallel_2}$. This 'two-step' Monte Carlo gives the desired shifts towards larger multiplicities and smaller rapidity, and results in a good agreement between Monte Carlo events and data (see Fig. 2).

The acceptance corrections for the cuts listed in subsection 3.3 are determined as follows.

1. Tracks and vertices out of the fiducial target volume arise from false tracking or off-target interactions. Whilst the first is evaluated by Monte Carlo comparison, the second is determined from a visual scan of 200 events; the combined correction, as a function of $(1 - x_F)$, is shown as $\varepsilon_{\text{vertex}}$ in Fig. 3.

2. The acceptance of the cuts on the forward energy and the longitudinal momentum loss are determined from Monte Carlo comparison, as well as the tracking efficiency for the leading proton as a function of $(1 - x_F)$ and t. The overall normalization of the tracking efficiency is obtained from a measurement with non-interacting beam tracks. (The combined correction is $\varepsilon_{\text{forward}}$ in Figs. 3a and 3b.)

3. Acceptance corrections for the cuts on backward energy and multiplicity are determined from Monte Carlo events ($\varepsilon_{\text{backward}}$). Only events with small masses, $M_X < 3.0$ GeV, are affected by these cuts. Nevertheless, $\varepsilon_{\text{backward}}$ contributes a large fraction of the total systematic error in the cross-section for two reasons: first, its value varies rapidly for small $(1 - x_F)$, where the cross-section is largest and corrections are most important. Secondly, little is known about the calorimeter response at very low energies, and its Monte Carlo simulation may not be completely accurate. The systematic error was estimated by varying the particle composition and multiplicity in the Monte Carlo simulation, adding a relative uncertainty of 15% to account for the unknown calorimeter response.

4. The acceptance of the rapidity gap condition at the trigger level is determined from data taken with the reference trigger 'INT', where the 'SP2' condition was not applied. The 'SP2' condition is unimportant for small values of $(1 - x_F)$, but as much as 50% of the diffractive events with large masses—and hence wider η-distributions—are rejected by it. The acceptance of the off-line cut on the η-gap in the drift chambers is evaluated by Monte Carlo comparison. It shows similar

behaviour as a function of $(1 - x_F)$, removing mostly high-mass diffractive events. The combined acceptance coefficient ε_{gap} is shown in Fig. 3.

Altogether, the selection cuts, including the trigger, remove about half of the diffractive events within the integration range, with a better acceptance at small values of t and $(1 - x_F)$. The largest corrections to the integrated cross-section stem from the tracking efficiency for the leading proton. The largest single contribution to the total systematic error arises from imposing a lower limit on the backward energy.

4 RESULTS ON THE DIFFRACTION CROSS-SECTIONS

4.1 The t-dependence of the diffraction cross-section

The differential cross-section $d\sigma/dt$ for the target nuclei Be, Al, and W is shown in Fig. 4. The values and their statistical errors are listed in Table 1. Within the range $0.01 \leq -t \leq 0.36$ $(\mathrm{GeV}/c)^2$ and the given errors, the spectra can be described by a parametrization

$$\frac{d\sigma}{dt} = C\, e^{-b|t|}.$$

The exponential fits yield $b = 6.22 \pm 0.36$ $(\mathrm{GeV}/c)^{-2}$ for Be, $b = 7.62 \pm 0.62$ $(\mathrm{GeV}/c)^{-2}$ for Al, and $b = 7.91 \pm 0.47$ $(\mathrm{GeV}/c)^{-2}$ for W. The χ^2 values of these fits, 9.89, 11.08, and 10.52 for Be, Al, and W, respectively, with 10 data points per fit, indicate that the simple exponential parametrization is fully adequate. The slope rises slowly with the nuclear mass: the difference between b(Be) and b(W) is about 4 standard deviations.

In order to obtain the dependence of the slope parameter on the mass M_X of the diffractively produced system, the data have been divided into bins of momentum loss $\Delta p_\parallel$, which is directly related to M_X (see subsection 3.2). In order to enhance the statistics for the high-mass region, data taken with the more selective triggers DF1 and DF2 (see subsection 3.1) are included for this analysis. The available background samples for inelastic and off-target interactions are too small to make a reliable background subtraction in each (t, M_X) bin, so this subtraction is not done in this analysis. The total contribution from this background is estimated to be less than 10%.

Figure 5 shows the distributions dN/dt for the beryllium data in six bins of M_X. All the spectra are consistent with the form $e^{-b|t|}$, and the results of fits for $0.01 \leq -t \leq 0.36$ $(\mathrm{GeV}/c)^2$ are given in the figure. This slope parameter is shown as a function of $(1 - x_F)$ for the Be and W data in Fig. 6. (The Al data sample is too small for this analysis.) The slopes for Be show a clear increase with $(1 - x_F)$ and hence M_X. The W data are consistent with a similar effect, but the statistics are poorer.

It should be noted that any residual background from inelastic and double-diffractive interactions will tend to decrease the slope parameter b with increasing M_X, since such

background increases with M_X and has a flatter t-distribution.

4.2 The x_F-dependence

Figure 7 shows the differential cross-section $d\sigma/dx_F$ for the nuclear targets Be, Al, and W; the corresponding values are listed in Table 2. The lines in Fig. 7 represent a fit to the data points with $(1 - x_F) > 0.015$, of the form $d\sigma/dx_F = C/(1 - x_F)$, a shape that gives a good description of pp diffraction at fixed t-intervals for masses M_X that are well above the region of nuclear resonances. The cut-off value $(1 - x_F) > 0.015$ corresponds to a mass threshold of $M_X > 3.5$ GeV.

The quality of the fit is not striking, especially for the lightest target nucleus, Be, and for large values of $(1 - x_F)$. The χ^2 values are 11.6, 5.8, and 18.7 for the seven data points of Be, Al, and W, respectively. By assuming a residual background component proportional to $(1 - x_F)$, the integrated background can be estimated from a two-parameter fit. The results are 0.6 mb for Be, 0.2 mb for Al, and -1.20 mb for W, within the systematic errors quoted for the diffraction cross-section in the next subsection.

4.3 The A-dependence of the integrated cross-section

The single-diffraction cross-section σ_{SD} for the reaction $pA \rightarrow pX$ is obtained from the differential cross-section $d^2\sigma/dx_F dt$ by integrating over the range of $x_F, 0 < (1 - x_F) < 0.075$, and over the four-momentum transfer in the range $0.01 < t < 0.36$ $(\mathrm{GeV}/c)^2$, and extrapolating over the remaining part of the t-region using the exponential fits indicated in Fig. 4. Figure 8 shows the results obtained for the target nuclei Be, Al, and W. Table 3 lists the values with their statistical and systematic errors. For comparison, Fig. 8 also contains the single-diffraction cross-section for proton–proton collisions, taking the average of the measurements by experiments at the CERN ISR [21],[22] and at FNAL [23], all at a similar centre-of-mass energy ($\sqrt{s}$ = 27.3–32.4 GeV). The pp cross-section is usually quoted as the sum of the cross-sections for the diffraction of either proton, and therefore has been divided by 2 to compare with the conditions of this experiment.

Figure 8 suggests a dependence of σ_{SD} on the nuclear target mass A of the form $\sigma_{SD} = \sigma_0 A^\alpha$. A fit through the data points for Be, Al, and W yields $\sigma_0 = 3.84\,\mathrm{mb} \pm 0.27\,\mathrm{mb}$ (stat.) $\pm 0.90\,\mathrm{mb}$ (syst.), and $\alpha = 0.35 \pm 0.02$ (stat.), with a χ^2 value of 2.02 for the three points. The error calculation of α considers only the statistical errors, since systematic effects will affect all data points in the same way and cancel in the calculation of α. Including the pp cross-section in the fit—and considering systematic errors as well—one obtains $\sigma_0 = 3.79\,\mathrm{mb} \pm 0.20\,\mathrm{mb}$ (stat.) $\pm 0.29\,\mathrm{mb}$ (syst.), and $\alpha = 0.35 \pm 0.02$ (stat.) ± 0.03 (syst.), with a χ^2 value of 2.09 for the four data points.

4.4 The fragmentation of the diffractively produced system

The investigation of the fragmentation of the diffractively produced state X provides more insight into the mechanism of diffraction excitation. Of the two fragmentation models proposed for proton diffractive excitation, i.e. the isotropic [24] and multiperipheral decay models [25], the latter is clearly favoured by recent pp and $p\bar{p}$ experiments [16],[26]. In the case of diffractive excitation of nuclei, the possible involvement of several nucleons would show up in the distributions of the particles emitted from X.

As already mentioned, the HELIOS set-up uses a combination of calorimeters and drift chambers to detect the charged and neutral particles produced by the diffractively excited nucleus. The reconstruction efficiency as a function of pseudorapidity η, rapidity y, and particle momentum p has been carefully studied by Monte Carlo simulation, and appropriate corrections have been applied to the raw data. However, as in this subsection we are not concerned with absolute cross-sections, but rather with the general properties of the diffractively produced system as a function of its mass and for different targets, the acceptance corrections ε_{cut} are irrelevant and have not been applied.

The $p_\perp$ distribution $\mathrm{d}N/\mathrm{d}p_\perp^2$ of the backward decay particles, for diffractive interactions with Be nuclei and integrated over all masses M_X, is shown in Fig. 9a. It reveals an exponential shape with two components, of which the steeper one is important at $p_\perp < 250$ MeV/c and is due to photons from π^0 decays, whereas the distribution above 250 MeV/c is dominated by charged pions. The average transverse momentum $\langle p_\perp \rangle$ is determined as the slope parameter of an exponential fit between 0.25 GeV/$c \leq p_\perp \leq$ 2.0 GeV/c, of the form

$$\frac{\mathrm{d}N}{\mathrm{d}p_\perp^2} = C\, \mathrm{e}^{-2p_\perp/\langle p_\perp \rangle}.$$

The results are shown as a function of the mass of the system M_X in Fig. 9b. In order to correct for overlapping particles that introduce spurious large transverse momenta, a separate calibration with Monte Carlo data was done for each mass bin. For masses larger than 3.0 GeV, $\langle p_\perp \rangle$ is constant with values between 320 and 360 MeV, as expected from multiperipheral decay models. (The isotropic decay model predicts an increase of $p_\perp$ with the mass M_X.) In the low-mass region $M_X < 3$ GeV, the models are indistinguishable since the average momentum is not high enough to reach the limitation in transverse phase space. The results for the $p_\perp$ spectra for the W target are very similar.

A typical pseudorapidity distribution, $\mathrm{d}N/\mathrm{d}\eta$, of the particles produced in the diffractive interaction, is shown in Fig. 2a. Corrections for the reconstruction efficiency as a function of η have been applied. It should be noted that the value of these corrections is rather sensitive to the details of the production of, and the calorimetric response to, low-energy particles with, for instance, kinetic energies of less than 50 MeV. In addition,

as already described in subsection 3.5, the selection cuts on diffractive events preferentially reject events with a wide η-distribution. The data cannot be easily corrected for this effect, but its importance has been evaluated from Monte Carlo calculations, and it is properly incorporated in comparisons between data and Monte Carlo.

The average multiplicity $\langle n \rangle$ of charged and neutral particles (photons), obtained as the integral of the distribution $\mathrm{d}N/\mathrm{d}\eta$, is shown in Fig. 10 as a function of M_{X} and for the target nuclei Be, Al, and W. All target nuclei show approximately the same behaviour of a steady increase with M_{X}. The multiplicity depends only weakly on the nuclear size; for the heaviest target, tungsten, the average multiplicity is only about 0.5 higher than for beryllium.

From the (pseudo) rapidity distributions we can also derive the mean values $\langle \eta \rangle$ and $\langle y \rangle$. In diffractive nucleon–nucleon interactions, the relation between the rapidity $\langle y \rangle$ of the diffractively produced system and the Feynman x_{F} of the leading proton is kinematically fixed:

$$\langle y \rangle \simeq \frac{1}{2} \log \frac{2(1 - x_{\mathrm{F}})p_0 + m_{\mathrm{p}}}{m_{\mathrm{p}}} .$$

In diffractive nucleon–nucleus interactions, this relation could vary if the number n_A of target nucleons involved is larger than one (replace m_{p} by $n_A m_{\mathrm{p}}$ in the above equation). Figure 11 shows the average rapidity and pseudorapidity measured as a function of $(1 - x_{\mathrm{F}})$ for the three target nuclei. Qualitatively, the x_{F}-dependence exhibits the expected behaviour: the mean rapidity and pseudorapidity rise approximately logarithmically with $(1 - x_{\mathrm{F}})$. The observed differences between the three target nuclei are small. On the average, the values for the lightest nucleus, beryllium, are 0.05 to 0.10 units larger than for tungsten.

The rapidity values $\langle y \rangle$ are about 0.3 units smaller than the pseudorapidity $\langle \eta \rangle$, owing to the contribution of low-energy particles. The error bars indicate the statistical errors, which are determined from the width and the number of entries of the individual distributions. The systematic errors (0.15 for $\langle \eta \rangle$, 0.25 for $\langle y \rangle$)—mainly due to the acceptance limitations for $\eta < -0.1$ and for very low energy particles—can only lead to a global shift of all the measured points and do not affect the shape of the correlation curves. Systematic errors also cancel in the relative comparison between curves.

We have compared our measurements on pseudorapidity, rapidity, and multiplicity—all as a function of $(1 - x_{\mathrm{F}})$—with the results obtained from Monte Carlo simulations made with the various generators for the fragmentation as described in subsection 3.5. The simulation includes the trigger, the detector response, and the off-line selection. It appears that all generators fail to describe the data, in that the generators give $\langle \eta \rangle$ and $\langle y \rangle$ consistently too high by 0.3 to 0.4 units, and $\langle n \rangle$ too low by 40%.

Plausible physical explanations are re-interactions of the excited target nucleon(s)

or of secondary particles within the same nucleus. The latter mechanism is found to be particularly important at nucleon energies below 3–5 GeV and at rapidities $y \leq 2$ in the laboratory frame. Net effects are a backward shift of the mean (pseudo) rapidity ($\langle\eta\rangle, \langle y\rangle$) and a higher multiplicity [19] depending, in magnitude, on the nuclear mass and the impact parameter of the collision. Investigating peripheral collisions with Be and W nuclei, we find sizeable effects for W only. However, the fact that the measured differences between heavy and light target nuclei are small, shows that intranuclear cascading, as it is at present understood and modelled in the Monte Carlo program, does not achieve consistency with the data. The differences between Be and W, on the other hand, can be well explained by modelling re-interactions of the excited nucleon based on a geometrical model of nuclear interactions [26].

5 SUMMARY AND DISCUSSION

In this experiment, high-mass diffractive excitation of nuclei has been measured for the first time in proton–nucleus collisions. The cross-section of this process is proportional to the nuclear radius, $\sigma_{\rm SD} \propto A^{1/3}$. This suggests that diffractive dissociation of nuclei is a peripheral process, predominantly involving nucleons on the rim of the nucleus. Such a result appears to be a natural consequence of the known peripherality of proton diffractive excitation, in the framework of optical models. However, it is less obvious how Pomeron exchange models with, for instance, coupling to quarks within individual nucleons [28],[29] would lead to an $A^{1/3}$-dependence of the cross-section.

The differential cross-section $\mathrm{d}\sigma/\mathrm{d}t$ was measured down to very small t-values, $0.01 \leq -t \leq 0.40$ $(\mathrm{GeV}/c)^2$. An exponential parametrization of the form $\mathrm{d}\sigma/\mathrm{d}t \propto \exp(bt)$ gives a good description of the data with values for the slope parameter b of 6.22, 7.62, and 7.91 $(\mathrm{GeV}/c)^{-2}$ for Be, Al, and W, respectively, which are close to the value for proton diffractive dissociation, $b_{\rm p} = 6.2$ $(\mathrm{GeV}/c)^{-2}$, in pp collisions at similar centre-of-mass energy, $\sqrt{s} = 30$ GeV [21]. Again, on the one hand, such a similarity is expected from optical models, which predict a t-slope that is independent of the size of the excited particle. On the other hand, particle-exchange models already fail to describe the pp inelastic diffraction cross-section at small values of t: they predict a turnover at small t and a vanishing cross-section for $t \to 0$ [29]. For larger t, an exponential slope is predicted [29], but its value is only about half the measured one. No predictions are at present available for pA collisions from the latter models.

The slope of the differential cross-section $\mathrm{d}\sigma/\mathrm{d}t$ shows a small increase with the nuclear mass A. The Be target data, which has the highest statistics, also shows a small increase with the excitation mass $M_{\rm X}$. For pp interactions, the CHLM Collaboration [21] found a constant slope parameter b as a function of $M_{\rm X}$, for masses larger than 3 GeV.

(Note that our experiment has no sensitivity to the very low mass region where the CHLM experiment measured a steep rise of b.) The observed increase with A and M_X, although small, deserves a closer examination. The Pomeron-exchange model predicts a decreasing slope for increasing mass M_X. This is already in conflict with the pp data, so one may expect that the model will also have difficulty in explaining an increasing slope for increasing nuclear mass A and excitation mass M_X. Optical models relate the slope parameter to the range of the interaction, e.g. in the model of Miettinen and Pumplin [3] to the range of the parton interaction. Thus a higher diffractive slope b implies an increased interaction range. Such a variation of the interaction range with nuclear mass and excitation mass is rather surprising, and confirmation by a further experiment would be desirable.

Our study of the decay properties of the diffractively excited nucleus has revealed similarities with the known characteristic features of the decay of diffractively excited protons [16],[26]: the phase-space distribution is longitudinal; the transverse-momentum spectra have an exponential shape; the mean transverse momentum is independent of the mass M_X. Moreover, all these features are similar to those of non-diffractive inelastic hadron collisions. In order to make a more quantitative comparison with inelastic pp collisions, we compared our data with Monte Carlo simulations based on fragmentation models that describe pp data in the relevant energy range ($\sqrt{s} = M_X$). The mean pseudorapidity $\langle\eta\rangle$ and rapidity $\langle y\rangle$ are lower by about 0.4 units than the Monte Carlo expectations, and the observed average multiplicity of particles is higher by about 40%. We consider these discrepancies to be indicative of intranuclear effects, which are not properly treated in the Monte Carlo generators. We note also that the simulation of the calorimeter response to very low energy particles is delicate.

Our results for the final-state particle distributions are remarkably insensitive to the mass of the target nucleus. Mean pseudorapidity, mean rapidity, and multiplicity, plotted as a function of $(1 - x_F)$, show the same behaviour for Be, Al, and W. This strongly suggests that the dominant process is the diffractive excitation of single nucleons, an observation which is supported by the $A^{1/3}$-dependence of the diffraction cross-section.

Acknowledgements

The correspondence with J.D. Bjorken on this subject, prior to the experiment, is acknowledged. The HELIOS Collaboration wishes to thank the staff of the PS–SPS accelerator complex for their excellent work in providing the very high quality particle beam. We acknowledge the valuable contributions of the technical staff of CERN and the collaborating institutes. The support of the national science and research foundations is gratefully acknowledged.

References

[1] G. Alberi and G. Goggi, Phys. Rep. **74** (1981) 1.

[2] K. Goulianos, Phys. Rep. **101** (1983) 169.

[3] H.I. Miettinen and J. Pumplin, Phys. Rev. **D8** (1978) 1696.

[4] C. Bemporad et al., Nucl. Phys. **B33** (1971) 397 and **B42** (1972) 627.
P. Mühlemann et al., Nucl. Phys. **B59** (1973) 106.

[5] M.A. Faessler, Nucl. Phys. **A447** (1986) 455 and Proc. 18th Int. Symposium on Multiparticle Dynamics, Tashkent (USSR), 1987, eds. I. Dremin and K. Goulamov (World Scientific, Singapore, 1988), p. 319.

[6] H. Gordon et al., Proposal to the SPSC: Lepton production, CERN–SPSC/P189 (1983).

[7] H. Gordon et al., Proposal to the SPSC: Study of high-energy densities over extended nuclear volumes via n–n collisions at the SPS, CERN–SPSC/P203 (1984).

[8] R. Beuttenmuler et al., Nucl. Instrum. Methods **A242** (1986) 471.

[9] D. Bettoni et al., Nucl. Instrum. Methods **A252** (1986) 272.

[10] T. Åkesson et al., Z. Phys. **C38** (1988) 383.

[11] T. Åkesson et al., Nucl. Instrum. Methods **A262** (1987) 243.

[12] C.W. Fabjan, Contributed paper No. 775 to the 24th Int. Conf. on High-Energy Physics, Munich, 1988, eds. R. Kotthaus and J.H. Kühn (Springer-Verlag, Berlin-Heidelberg, 1989).

[13] T. Inami and R.G. Roberts, Nucl. Phys. **B93** (1975) 497.

[14] J.P. Pansart, DPhPE 86–06, CEN–Saclay, France (1986).

[15] V. Innocente, A. Capella, V. Ramello and J. Tran Thanh Van, Phys. Lett. **B169** (1986) 285.

[16] R.E. Ansorge et al., Z. Phys. **C33** (1986) 175.

[17] D. Bernard et al., Phys. Lett. **B186** (1987) 227.

[18] F.E. Paige and S.D. Protopopescu, Brookhaven report BNL 31987 (1982) and Proc. DPF Summer Study on Elementary Particle Physics and Future Facilities, Snowmass, Colo., 1982, eds. R. Donaldson, R. Gustafson and F. Paige (AIP, New York, 1983), p. 471.

[19] J. Ranft, private communication; Program AAEVT, Version 12/88 (1988).
J. Ranft, preprint CERN TIS–RP 219 PP (1988), submitted to Z. Phys. C.

[20] H. En'yo, Univ. Tokyo report UTPN–200 (1985).

[21] M.G. Albrow et al., Nucl. Phys. **B108** (1976) 1.

[22] J.C.M. Armitage et al., Nucl. Phys. **B194** (1982) 365.

[23] J. Schamberger et al., Phys. Rev. **D17** (1978) 1268; Phys. Rev. Lett. **34** (1975) 1121.

[24] R.C. Hwa, Phys. Rev. Lett. **26** (1971) 1143.
M. Jacob and R. Slansky, Phys. Rev. **D5** (1972) 1847.

[25] D. Amati, A. Stanghellini and S. Fubini, Nuovo Cimento **26** (1962) 897.
G.C. Fox, *in* High-Energy Collisions, Stony Brook, 1973, ed. C. Quigg (AIP Conf. Proc. **15**, No. 7, New York, 1973), p. 180.

[26] A.M. Smith et al., Phys. Lett. **B163** (1985) 267.

[27] A.D. Jackson and H. Bøggild, Nucl. Phys. **A470** (1987) 669.

[28] A. Donnachie and P.V. Landshoff, Nucl. Phys. **B244** (1984) 322.

[29] G. Ingelman and P.E. Schlein, Phys. Lett. **B152** (1985) 256.

Table 1

Differential diffraction cross-section $d\sigma/dt$ of the reaction $pA \rightarrow pX$, integrated over $(1 - x_F) < 0.075$, for the three nuclear targets.

$\lvert t \rvert$ $[(\mathrm{GeV}/c)^2]$	t-bin half width $[(\mathrm{GeV}/c)^2]$	$d\sigma_{SD}/dt$ $[\mathrm{mb}/(\mathrm{GeV}/c)^2]$	Error $[\mathrm{mb}/(\mathrm{GeV}/c)^2]$
Beryllium			
0.020	0.010	46.62	3.25
0.040	0.010	37.69	3.33
0.066	0.015	33.10	1.68
0.097	0.015	31.08	1.65
0.128	0.015	22.85	1.69
0.162	0.020	16.45	1.34
0.203	0.020	14.73	1.36
0.245	0.020	9.20	1.78
0.290	0.025	9.53	1.27
0.341	0.025	7.28	1.31
Aluminium			
0.020	0.010	98.15	9.21
0.040	0.010	56.70	8.71
0.065	0.015	60.41	5.27
0.095	0.015	45.12	4.38
0.128	0.015	35.46	5.04
0.163	0.020	33.88	4.60
0.204	0.020	20.32	4.03
0.241	0.020	11.39	2.92
0.288	0.025	13.61	3.12
0.343	0.025	10.84	3.74
Tungsten			
0.020	0.010	169.65	10.85
0.040	0.010	136.45	11.04
0.066	0.015	98.78	7.29
0.097	0.015	91.58	5.67
0.126	0.015	59.32	6.39
0.161	0.020	48.53	5.16
0.205	0.020	41.96	5.56
0.243	0.020	28.95	5.89
0.291	0.025	17.23	4.18
0.339	0.025	15.96	4.46

Table 2

Differential diffraction cross-section $d\sigma/dx_F$ for the reaction pA $\rightarrow$ pX, integrated over t, for the three nuclear targets.

$(1-x_F)$	x_F-bin half width	$d\sigma_{SD}/dx_F$ (mb)	Error (mb)
Beryllium			
0.002	0.002	212.6	11.6
0.007	0.002	219.5	11.4
0.011	0.002	173.7	12.7
0.017	0.003	153.2	9.2
0.023	0.003	121.9	8.7
0.031	0.004	95.8	8.5
0.040	0.004	85.7	9.2
0.050	0.006	62.6	11.5
0.061	0.006	7.9	9.2
0.072	0.006	67.7	11.7
Aluminium			
0.002	0.002	369.9	42.6
0.007	0.002	346.1	41.8
0.011	0.002	282.9	41.7
0.017	0.003	259.2	31.7
0.023	0.003	210.8	29.8
0.031	0.004	156.2	25.7
0.041	0.004	135.8	24.6
0.050	0.006	123.7	26.4
0.061	0.006	69.3	19.8
0.071	0.006	76.4	26.3
Tungsten			
0.002	0.002	1042.7	68.4
0.007	0.002	883.4	62.1
0.011	0.002	656.0	64.8
0.016	0.003	509.5	51.3
0.023	0.003	320.2	41.2
0.031	0.004	292.3	41.0
0.040	0.004	153.8	33.1
0.050	0.006	106.8	30.1
0.061	0.006	49.3	23.0
0.072	0.006	60.1	32.4

Table 3

Single-diffraction cross-section for pA $\rightarrow$ pX, integrated over t and $(1 - x_F) < 0.075$ for three nuclear targets.

Target	Cross-section (mb)	Stat. error (mb)	System. error (mb)
Beryllium ($A = 9$)	8.21	0.30	1.18
Aluminium ($A = 27$)	13.29	0.80	1.84
Tungsten ($A = 184$)	23.52	1.09	3.36

Figure captions

Fig. 1: Top view of the HELIOS spectrometer with the components used in this experiment. The inset shows an enlarged view of the target area (vertical dimensions are not to scale).

Fig. 2: Comparison of a) pseudorapidity and b) multiplicity distributions for data (minimum-bias diffractive trigger sample, Be target) and for the phenomenological 'two-step' Monte Carlo simulation.

Fig. 3: Acceptance correction coefficients for diffractive events as a function of a) $(1 - x_F)$, integrated over $0.01 \leq t \leq 0.36\,(\mathrm{GeV}/c)^2$; b) t, integrated over $(1 - x_F) < 0.075$.

Fig. 4: Differential diffraction cross-section $\mathrm{d}\sigma/\mathrm{d}t$ of the reaction pA $\rightarrow$ pX, integrated over $(1 - x_F) < 0.075$, for the nuclear targets Be, Al, and W. The lines are exponential fits to the data points, giving the indicated slope parameters b.

Fig. 5: Four-momentum transfer distributions of the reaction pBe $\rightarrow$ pX, for six different bins of the excitation mass M_X. The lines are exponential functions fitted to the data points, giving the indicated slope parameters b.

Fig. 6: Slope parameters b of the exponential fits to the distributions $\mathrm{d}N/\mathrm{d}t$ of the reaction pA $\rightarrow$ pX, for Be and W nuclei, as a function of $(1 - x_F)$.

Fig. 7: Differential diffraction cross-section $\mathrm{d}\sigma/\mathrm{d}x_F$ for the reaction pA $\rightarrow$ pX, integrated over t, for the nuclear targets Be, Al, and W. The lines are fits to data points, as explained in the text.

Fig. 8: Single-diffraction cross-section for the reaction pA $\rightarrow$ pX, integrated over t and $(1 - x_F) < 0.075$, for the nuclear targets A = p, Be, Al, and W. The pp cross-section is averaged over the results given in Refs. [21], [22], and [23]. Error bars indicate statistical errors; brackets, systematic errors.

Fig. 9: a) $p_\perp$ distribution and b) average $p_\perp$ of the particles produced in the fragmentation of the diffractively excited system as a function of its mass M_X, for the diffraction of Be nuclei.

Fig. 10: Average total (charged and neutral) multiplicity of particles produced in the fragmentation of the diffractively excited system as a function of its mass M_X, for the target nuclei Be, Al, and W.

Fig. 11: a) Mean pseudorapidity and b) mean rapidity of the diffractively produced system X as a function of $(1 - x_F)$, for the target nuclei Be, Al, and W.

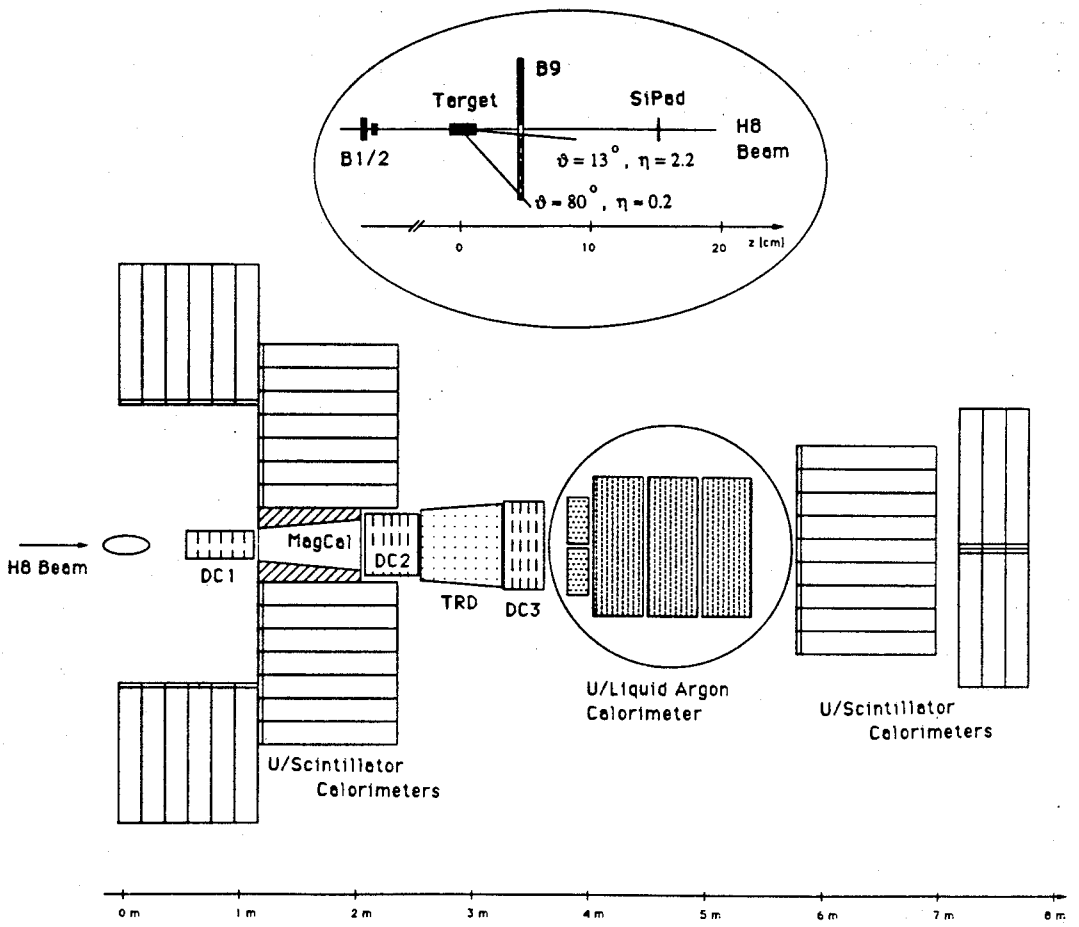
B9
Target
SiPad
H8 Beam
B1/2
ϑ = 13°, η = 2.2
ϑ = 80°, η = 0.2
0
10
20
z [cm]
H8 Beam
DC1
MagCal
DC2
TRD
DC3
U/Liquid Argon Calorimeter
U/Scintillator Calorimeters
U/Scintillator Calorimeters
0 m
1 m
2 m
3 m
4 m
5 m
6 m
7 m
8 m

Fig. 1

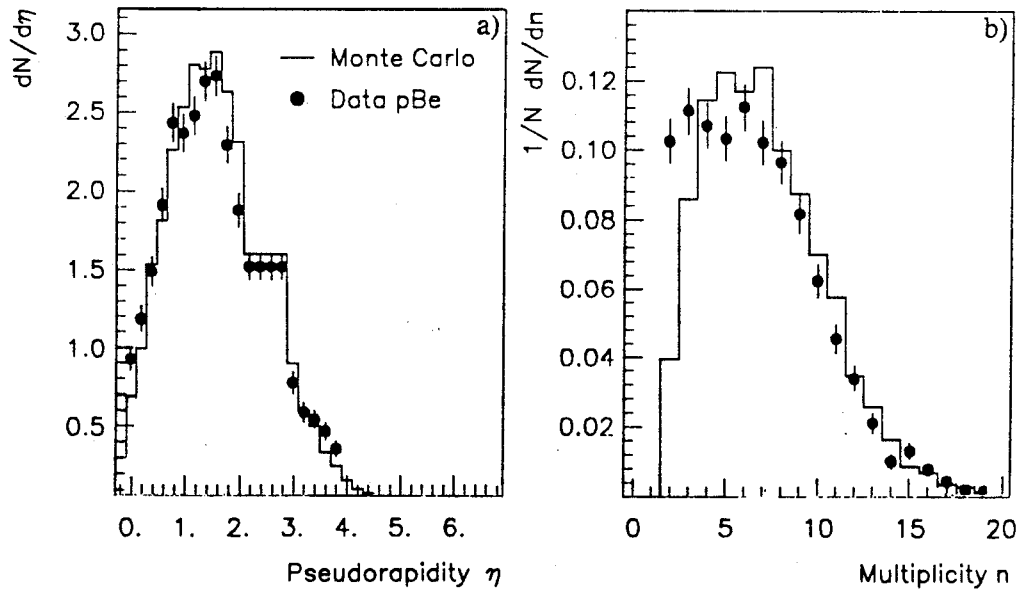
a)
Monte Carlo
Data pBe
dN/dη
3.0
2.5
2.0
1.5
1.0
0.5
0. 1. 2. 3. 4. 5. 6.
Pseudorapidity η
b)
1/N dN/dn
0.12
0.10
0.08
0.06
0.04
0.02
0 5 10 15 20
Multiplicity n

Fig. 2

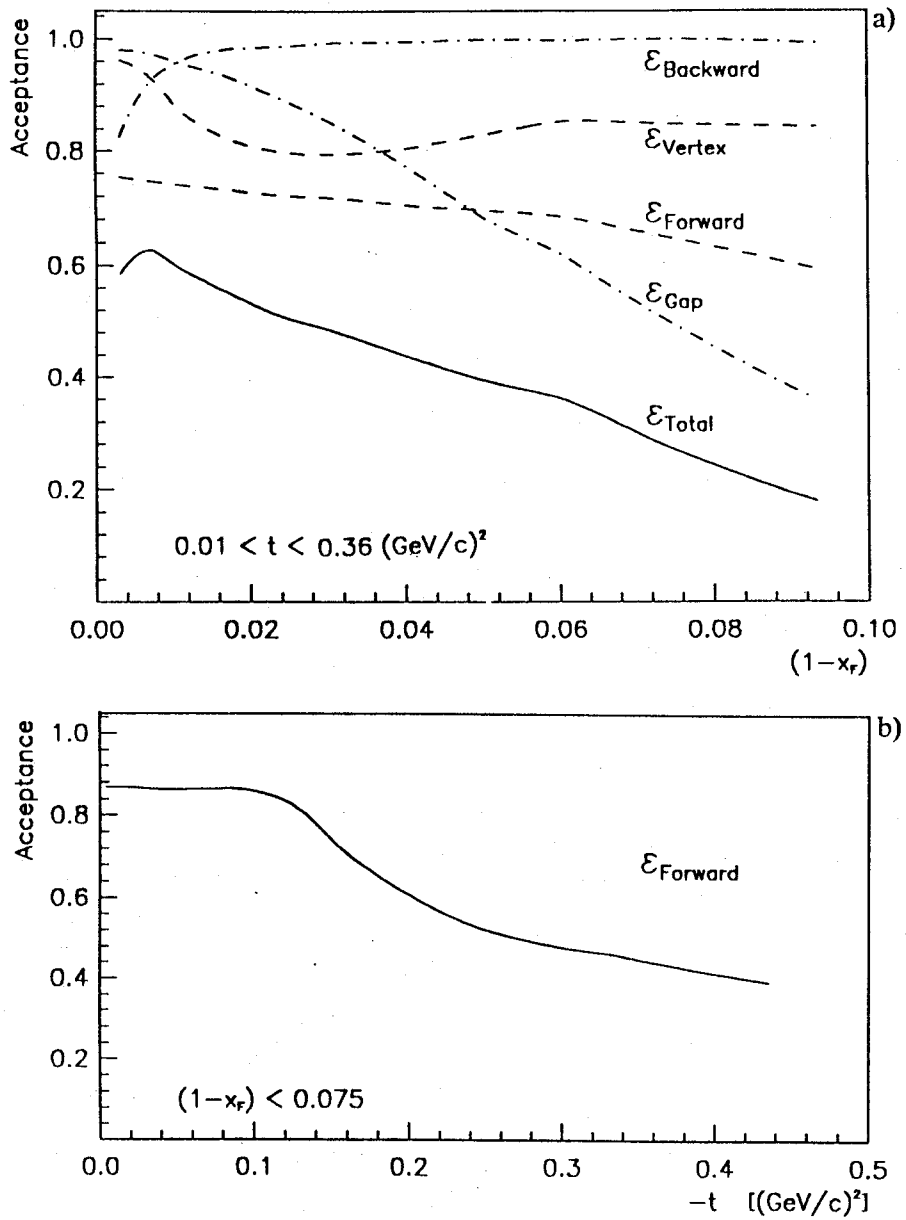
a)
Acceptance
1.0
0.8
0.6
0.4
0.2
$\varepsilon_{Backward}$
ε_{Vertex}
$\varepsilon_{Forward}$
ε_{Gap}
ε_{Total}
0.01 < t < 0.36 (GeV/c)²
0.00
0.02
0.04
0.06
0.08
0.10
$(1-x_F)$
b)
Acceptance
1.0
0.8
0.6
0.4
0.2
$\varepsilon_{Forward}$
$(1-x_F) < 0.075$
0.0
0.1
0.2
0.3
0.4
0.5
$-t$ [(GeV/c)²]

Fig. 3

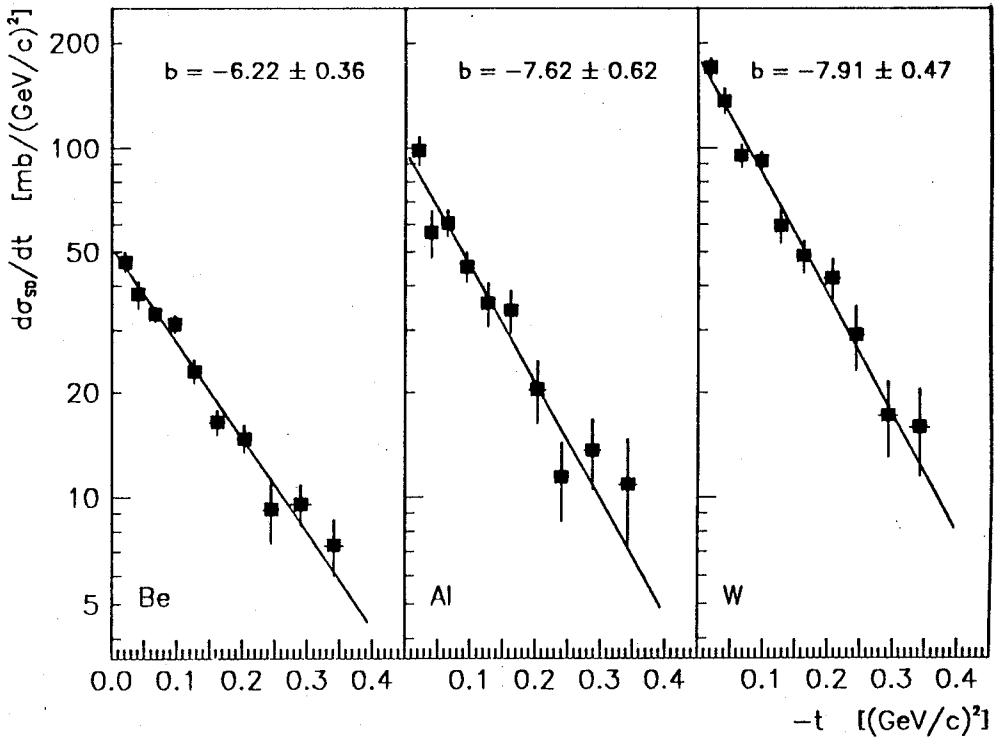
$d\sigma_{sa}/dt$ [mb/(GeV/c)²]
200
100
50
20
10
5
b = −6.22 ± 0.36
b = −7.62 ± 0.62
b = −7.91 ± 0.47
Be
Al
W
0.0
0.1
0.2
0.3
0.4
$-t$ [(GeV/c)²]

Fig. 4

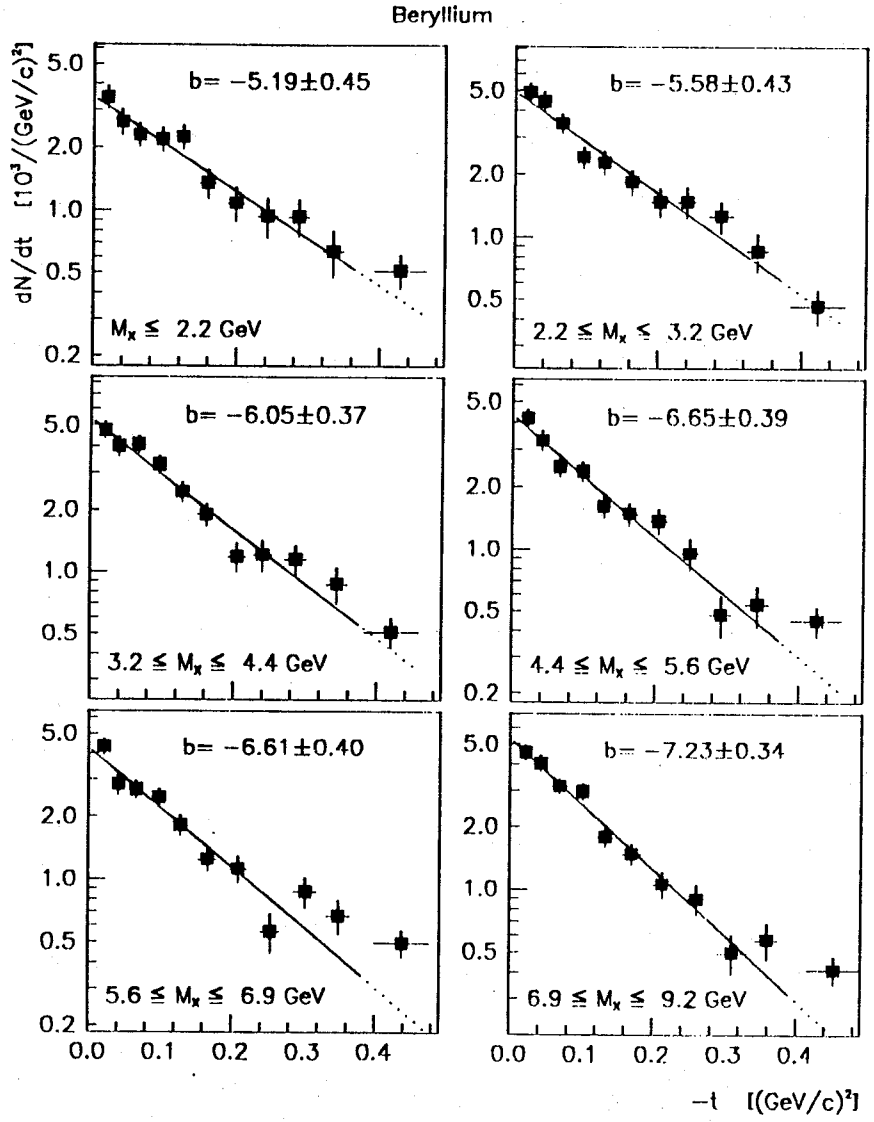
Beryllium
dN/dt [10³/(GeV/c)²]
b= −5.19±0.45
M_x ≤ 2.2 GeV
b= −5.58±0.43
2.2 ≤ M_x ≤ 3.2 GeV
b= −6.05±0.37
3.2 ≤ M_x ≤ 4.4 GeV
b= −6.65±0.39
4.4 ≤ M_x ≤ 5.6 GeV
b= −6.61±0.40
5.6 ≤ M_x ≤ 6.9 GeV
b= −7.23±0.34
6.9 ≤ M_x ≤ 9.2 GeV
−t [(GeV/c)²]

Fig. 5

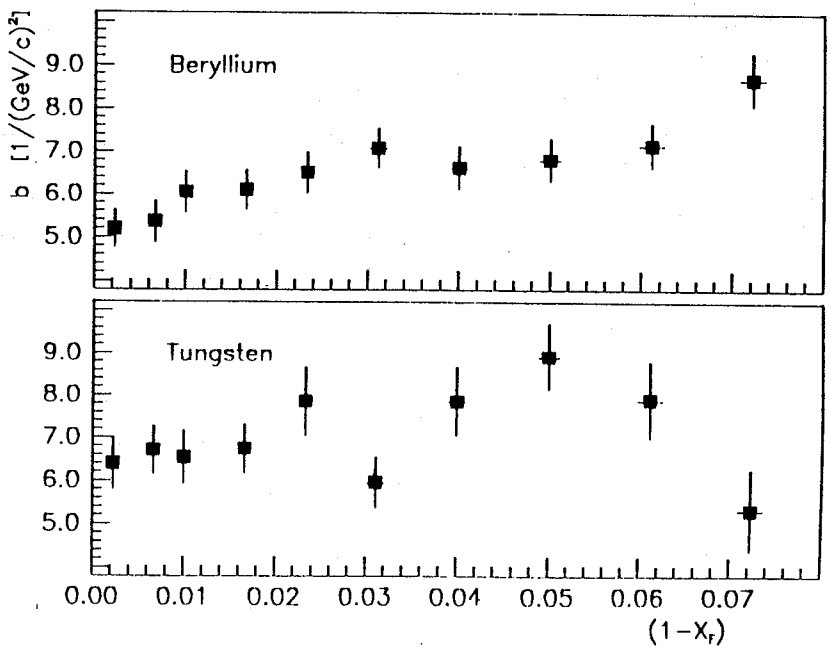
b [1/(GeV/c)²]
Beryllium
Tungsten
(1−X_F)

Fig. 6

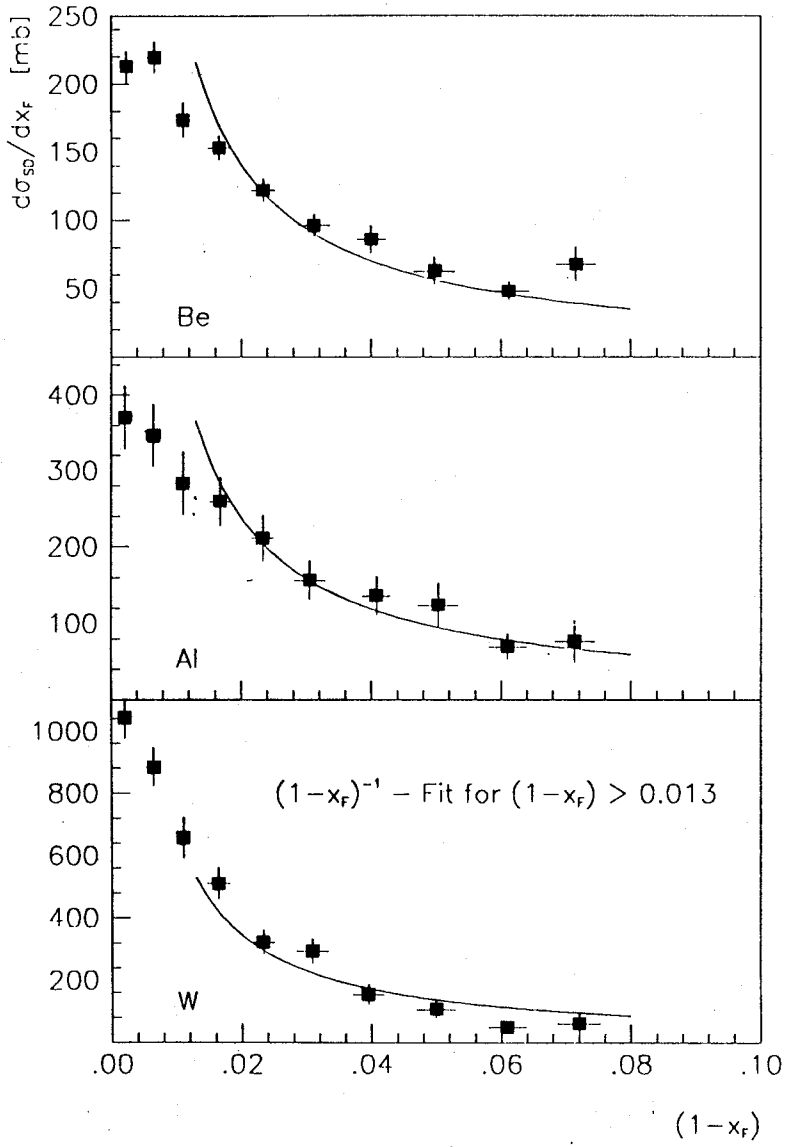
$d\sigma_{SD}/dx_F$ [mb]
250
200
150
100
50
Be
400
300
200
100
Al
1000
800
600
400
200
W
$(1-x_F)^{-1}$ – Fit for $(1-x_F) > 0.013$
.00
.02
.04
.06
.08
.10
$(1-x_F)$

Fig. 7

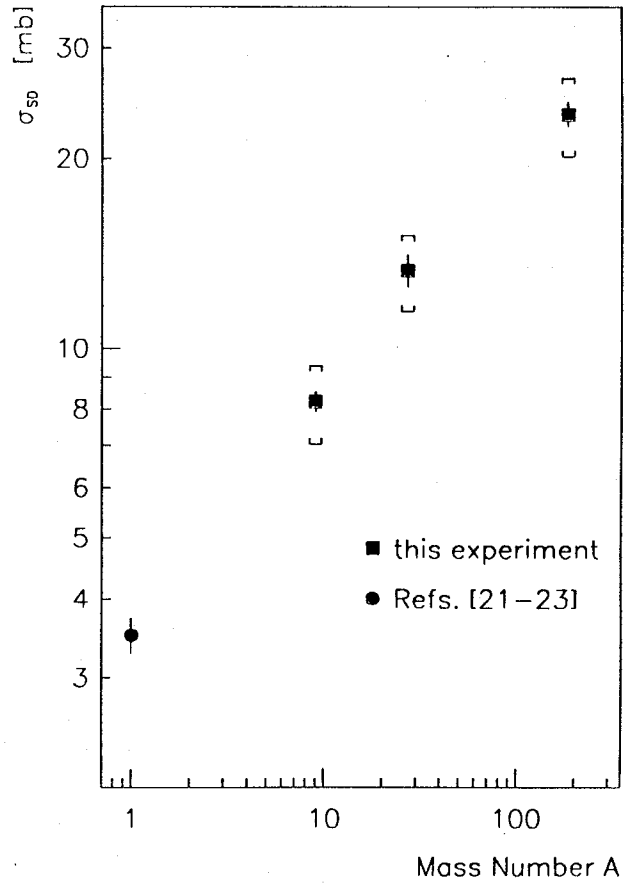
σ_{SD} [mb]
30
20
10
8
6
5
4
3
this experiment
Refs. [21–23]
1
10
100
Mass Number A

Fig. 8

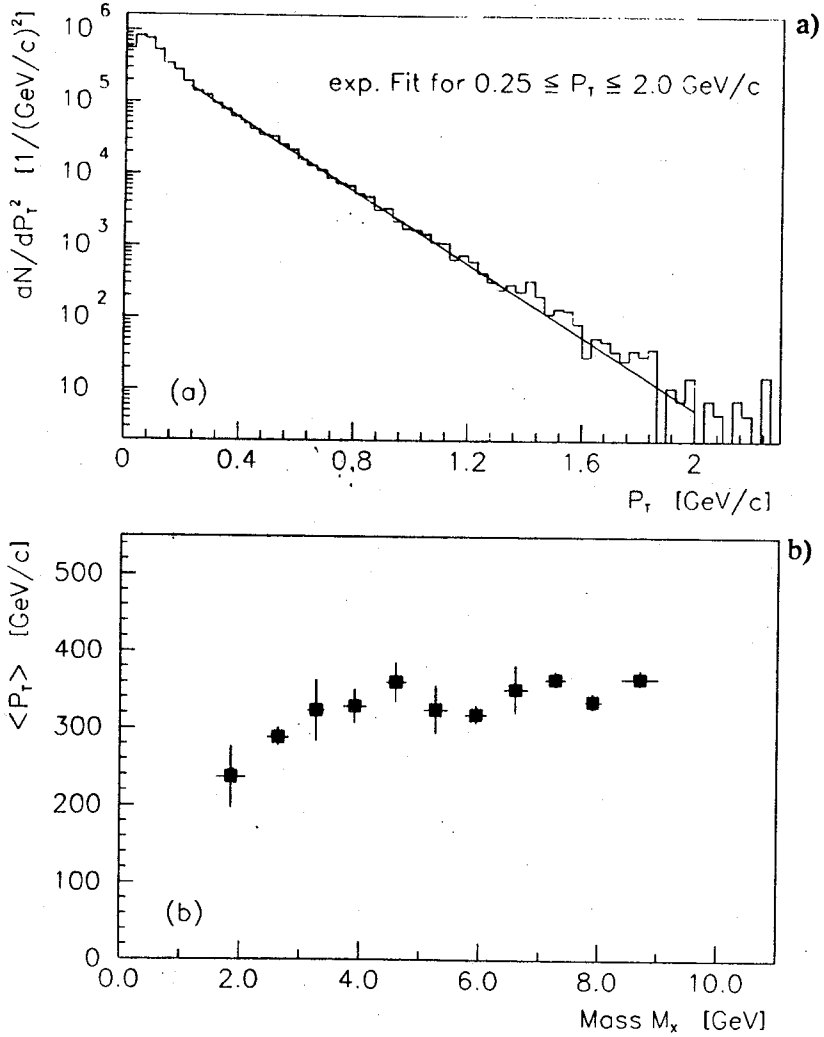
a)
exp. Fit for 0.25 ≤ P_T ≤ 2.0 GeV/c
dN/dP_T^2 [1/(GeV/c)^2]
(a)
P_T [GeV/c]
b)
$<P_T>$ [GeV/c]
(b)
Mass M_x [GeV]

Fig. 9

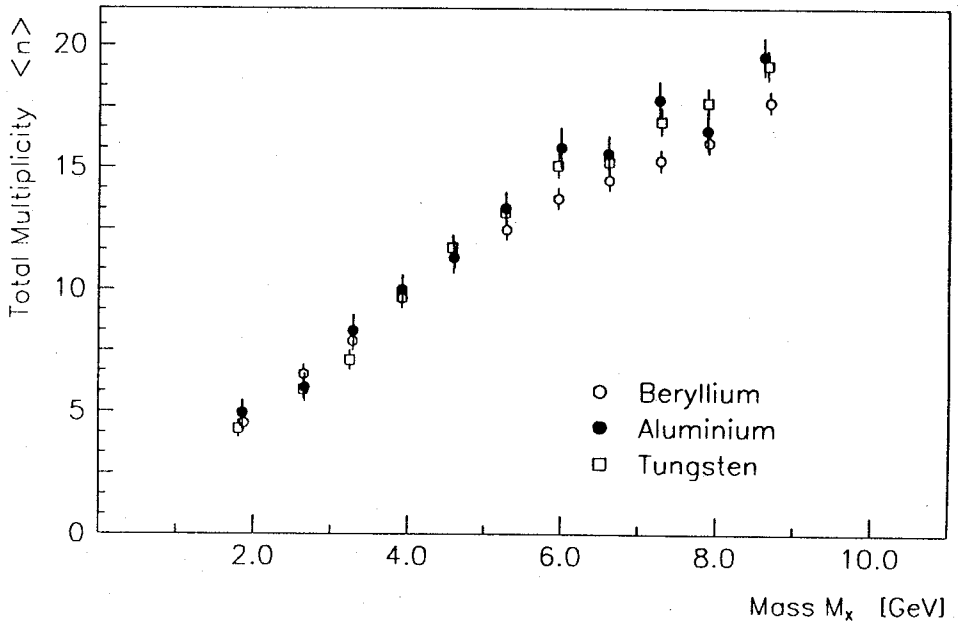
Total Multiplicity <n>
Beryllium
Aluminium
Tungsten
Mass M_x [GeV]

Fig. 10

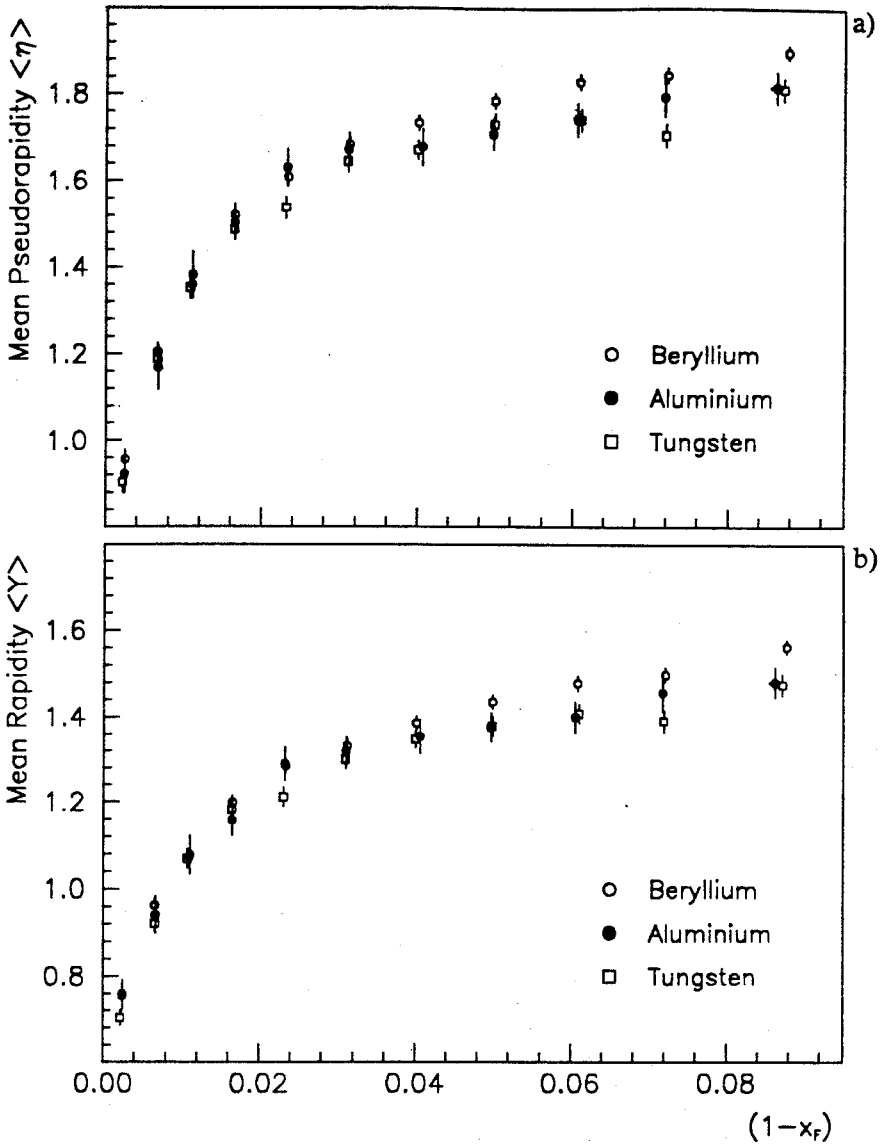

Fig. 11

Imprimé au CERN. Prix : 0.95 Fr.